The Astrophysical Journal Letters, 922:L18 (5pp), 2021 November 20 https://doi.org/10.3847/2041-8213/ac36cf


# Turbulent Magnetogenesis in a Collisionless Plasma

F. Pucci[1,2], M. Viviani[3], F. Valentini[3], G. Lapenta[2], W. H. Matthaeus[4], and S. Servidio[3]
[1] Istituto per la Scienza e Tecnologia dei Plasmi, Consiglio Nazionale delle Ricerche (ISTP-CNR), Via Amendola 122/D, I-70126 Bari, Italy; francesco.pucci@istp.cnr.it
[2] Centre for Mathematical Plasma Astrophysics, Department of Mathematics, KU Leuven, Celestijnenlaan 200B, B-3001 Leuven, Belgium
[3] Dipartimento di Fisica, Università della Calabria, I-87036 Cosenza, Italy
[4] Department of Physics and Astronomy, University of Delaware, Newark, DE 19716, USA
*Received 2021 October 4; revised 2021 October 15; accepted 2021 November 4; published 2021 November 19*

## Abstract

We demonstrate an efficient mechanism for generating magnetic fields in turbulent, collisionless plasmas. By using fully kinetic, particle-in-cell simulations of an initially nonmagnetized plasma, we inspect the genesis of magnetization, in a nonlinear regime. The complex motion is initiated via a Taylor–Green vortex, and the plasma locally develops strong electron temperature anisotropy, due to the strain tensor of the turbulent flow. Subsequently, in a domino effect, the anisotropy triggers a Weibel instability, localized in space. In such active wave–particle interaction regions, the seed magnetic field grows exponentially and spreads to larger scales due to the interaction with the underlying stirring motion. Such a self-feeding process might explain magnetogenesis in a variety of astrophysical plasmas, wherever turbulence is present.

*Unified Astronomy Thesaurus concepts:* Interstellar magnetic fields (845); Interstellar medium (847); Plasma astrophysics (1261); Plasma physics (2089)

## 1. Introduction

Magnetic fields permeate the universe, but their origin still represents an open question (Kulsrud & Zweibel 2008), despite years of studies (see Widrow et al. 2012 and references therein). The magnetic fields of most stars and galaxies are believed to be sustained and amplified by hydromagnetic dynamo action (Parker 1970), an essential element of which is turbulence (Kraichnan & Nagarajan 1967; Pouquet et al. 1976; Mininni et al. 2003; Brandenburg 2018). In turn, turbulent motion is stirred by the evolution of baryonic and dark matter, with stellar collisions being suggested as a possible mechanism for increasing local shearing motions (Colgate et al. 2001). For extragalactic plasmas, dynamos in noncollisional and weakly collisional plasmas also have been investigated (Rincon et al. 2016; St-Onge & Kunz 2018; Rincon 2019; Pusztai et al. 2020; St-Onge et al. 2020). In such studies, various plasma instabilities contribute to dynamo action.

In the above scenarios, an initial seed of magnetic field is assumed. It is therefore essential to demonstrate the origin of such seeds from which magnetic fields can emerge and grow as we can observe them today on large and small scales. The generation of seed magnetic fields—the problem of magnetogenesis—is addressed in this paper, and is relevant not only in astrophysics but also in laboratory settings such as laser-plasma experiments (Schoeffler et al. 2016). Proposed explanations such as the Biermann battery rely on inertial responses of electrons and ions to a pressure gradient (Biermann 1950); however, in the case of weakly collisional media, a more efficient candidate for the magnetogenesis is the kinetic Weibel instability (Weibel 1959). This process, based on the instability of strongly anisotropic particle distribution functions, has been verified in a variety of simulations and plasma experiments (Huntington et al. 2015; Schoeffler & Silva 2020). Schlickeiser & Shukla (2003) considered a cosmological situation of structure formation, in the linear regime, from an initial configuration of two interpenetrating collisionless electron–ion streams.

As an alternative, in the present study we consider an initial vortex configuration, in the nonlinear regime, to drive the Weibel instability. In the collisionless case, it dominates the dynamics at small scales at $\ell \sim d_e$, where $d_e$ is the electron inertial length. Although such kinetic instability is a very powerful magnetic field source, it requires an existing highly non-Maxwellian plasma, namely, an ad hoc, unstable velocity distribution. In the Weibel scenario, such anisotropic distribution is a given ingredient.

More recently, in a sequence of inspiring works, it has been suggested that collisionless plasmas might develop large temperature anisotropy, and hence non-Maxwellian distributions, not only via an existing magnetic field but also via gradients of fluid-like variables. The temperature anisotropy can be generated via shearing motions in which gradients of the particle bulk velocities are present (Cerri et al. 2014; Del Sarto et al. 2016). In principle, the production of these anisotropies can make the plasma Weibel-unstable, with subsequent production of a small-scale magnetic field produced by growth and nonlinear saturation of the instability. However, this possibility has not been explored yet.

In this Letter, we establish a connection between the above elements and show the possibility that plasma turbulence provides locally strong velocity gradients, initiating the magnetogenesis. We inspect the generation of a magnetic field in an initially isotropic, Maxwellian plasma, with ions and electrons, via full-Vlasov simulations. We perturb such a collisionless system via a vortical motion. The chosen configuration immediately develops plasma turbulence. We note that, contrary to previous works, this is not a perturbed equilibrium but rather a fully nonlinear, nonstationary state. In the turbulent field, local shears initiate electron pressure

anisotropy, which subsequently drives the Weibel instability. In this chain reaction, the magnetic field is then amplified due to the kinetic plasma interaction with the turbulent, stirring flow.

## 2. Method

We solve numerically the Vlasov–Maxwell set of equations for a plasma made of of ions ($i$) and electrons ($e$), by using the fully kinetic semi-implicit particle-in-cell code iPic3D (Markidis et al. 2010). The computational domain is a cubic box of length $L = 20d_i$, and the number of cells is $512^3$. We use a reduced ion-to-electron mass ratio $m_i/m_e = 256$, resulting in a grid size $\Delta_{xyz} \simeq 0.6d_e \simeq 18\lambda_D$, where $d_e$ is the electron skin-depth and $\lambda_D$ is the Debye length. For the time step $\Delta t$, we chose $\Delta t = 0.0625\omega_{\rm pi}^{-1} = \omega_{\rm pe}^{-1}$, where $\omega_{\rm pi}$ and $\omega_{\rm pe}$ are the ion and electron plasma frequency, respectively. The initial velocity field is prescribed in the form of a Taylor–Green vortex (Taylor & Green 1937), with the bulk flow of particles described by

$$\begin{aligned} \boldsymbol{u}_s(x, y, z) = u_{s0}[&\sin(\kappa_0 x)\cos(\kappa_0 y)\cos(\kappa_0 z)\,\hat{\boldsymbol{e}}_x \\ &- \cos(\kappa_0 x)\sin(\kappa_0 y)\cos(\kappa_0 z)\,\hat{\boldsymbol{e}}_y], \end{aligned} \tag{1}$$

where $s = i, e$ indicates the particles species, $u_{i0} = u_{e0} = 0.03c$ is the large-scale flow, $c$ is the speed of light, and $\kappa_0 = 2\pi/L$. At the beginning of the simulation, the electric and magnetic fields are zero and the distributions of electrons and ions are Maxwellians with thermal speed $v_{{\rm th},e} = 0.035c$ and $v_{{\rm th},i} = 0.005c$, respectively. The density is uniform and the net charge is zero. We populate each cell with 500 particles. Periodic boundary conditions are used in all three Cartesian directions. Here we show results for the highest-resolution run, although we performed a convergence study by varying the mesh resolution and the number of particles per cell.

## 3. Results

The flow quickly develops complexity, producing small-scale eddies, thus establishing a fully turbulent cascade (Olshevsky et al. 2018). The upper panel in Figure 1 shows the time evolution of some relevant energy components, together with the total energy, which is well conserved. Beginning with the state described in Equation (1), the bulk kinetic energy of the flow decays, as expected in turbulence, producing smaller structures and perturbing the other fields. After an initial transient, the magnetic energy starts an exponential growth at $t \sim 800\omega_{\rm pe}^{-1}$.

To determine the characteristic spatial scale of the emerging magnetic field, we computed the isotropic magnetic energy spectra, as a function of $k$, at different times of the simulation. As it can be seen from Figure 1 (bottom), the energy starts growing at a fixed mode $k \simeq 0.6d_e^{-1}$, until $t = 1000\omega_{\rm pe}^{-1}$ (Schoeffler et al. 2016). After this fast growth phase, the magnetic energy increase is slower and is back-transferred in $k$, toward larger scales.

In order to understand the origin of $B$, we analyze the structure of the electron velocity distribution functions, in the absence of preferred directions (Servidio et al. 2012). We define the electron temperature anisotropy as

$$A_e = \left(\frac{2P_1^{(e)}}{P_2^{(e)} + P_3^{(e)}}\right) - 1, \tag{2}$$

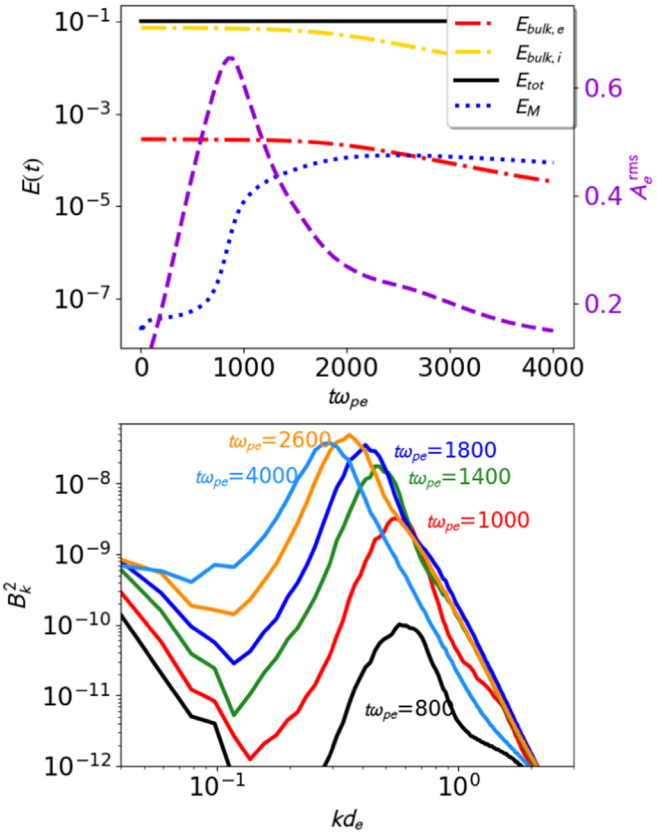


**Figure 1.** (Top) Time evolution of the total (black), ion–electron bulk kinetic (yellow and red), and magnetic (dot-blue) energies. Electron temperature anisotropy is represented with a (purple) dashed line, labeled on the right axis. (Bottom) Magnetic energy spectra at different times.

where $P_1 > P_2 > P_3$ are the eigenvalues derived from the diagonalization of the pressure tensor $P_{ij}$. We show the time evolution of the rms value of $A_e$ in Figure 1. It reveals a marked peak at $t \sim 900\omega_{\rm pe}^{-1}$, the time at which the magnetic energy attains its maximum production rate.

Figure 2 shows a 3D representation of the turbulent pattern at $t = 800\omega_{\rm pe}^{-1}$. The (colored) filled contours represent $|\boldsymbol{B}|$, emerging as patterns surrounded by the vortical flow (green streamlines). The patches are localized in particular regions of the volume, i.e., the magnetic field grows in between rolling vortexes. These structures resemble the typical snake-like filaments of the Weibel instability.

Starting from the induction equation, in order to understand the best candidate for the magnetic field amplification, we analyzed the separate contributions to the electric field curl coming from the generalized Ohm's law:

$$\begin{aligned} \boldsymbol{E} \sim &-\frac{1}{m_e n_i + m_i n_e}(m_e n_i \boldsymbol{v_i} + m_i n_e \boldsymbol{v_e}) \times \boldsymbol{B} \\ &+ \frac{m_e m_i}{e(m_e n_i + m_i n_e)}\nabla \cdot (n_i \boldsymbol{v_i}\boldsymbol{v_i} - n_e \boldsymbol{v_e}\boldsymbol{v_e}) \\ &+ \frac{m_e}{e(m_e n_i + m_i n_e)}\nabla \cdot P_i - \frac{m_i}{e(m_e n_i + m_i n_e)}\nabla \cdot \mathcal{P}_e. \end{aligned} \tag{3}$$

Note that here we neglected contributions from terms $\propto \frac{\partial}{\partial t}$, as these are small compared to the other terms. We estimated the strength of the curl of each term in Equation (3), by examining

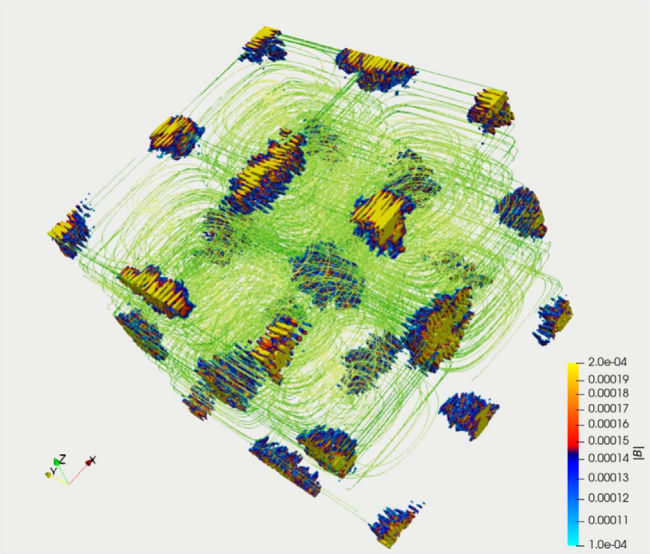


**Figure 2.** Rendering of the Taylor–Green turbulent field, with filled contours of the magnetic field $|\boldsymbol{B}|$ (colored patches) and streamlines of ions velocity (green) at $t = 800\omega_{\rm pe}^{-1}$.

the probability density functions (PDFs) of their absolute values, as shown in Figure 3. It is evident that the divergence of the electron pressure tensor is the source of the magnetic field perturbations, in agreement with the behavior of the anisotropy observed in Figure 1.

We show the PDFs of the different terms in Figure 3 at time $t = 400\omega_{\rm pe}^{-1}$. The relative magnitudes of the terms do not change and we do not show here the PDFs at following times. The $\nabla \times \nabla \cdot \mathcal{P}_e$ term is orders of magnitude larger than the others, indicating that electron anisotropy is the leading cause of the electric field generation.

We propose a mechanism for the generation of the pressure anisotropy as follows. Integrating the Vlasov equations, one can obtain the evolution equation for the pressure tensor. In accordance with the earliest stage of the unmagnetized Taylor–Green vortex, assuming for simplicity a zero heat flux closure and neglecting the electromagnetic contribution, one finds (Del Sarto et al. 2016)

$$\frac{\partial \mathcal{P}_{ij}}{\partial t} \sim -\left[\frac{\partial u_k \mathcal{P}_{ij}}{\partial x_k} + \mathcal{P}_{kj}\frac{\partial u_i}{\partial x_k} + \mathcal{P}_{ik}\frac{\partial u_j}{\partial x_k}\right], \tag{4}$$

where $u_j$ is the bulk velocity. The above approximation is true at leading order, for both species, although electrons are of central interest, since they carry currents. Assuming an initially Maxwellian distribution, $\mathcal{P}_{ij} = P\delta_{ij}$ ($P$ being the isotropic pressure), and an incompressible flow, Equation (4) simplifies to

$$\frac{\partial \mathcal{P}_{ij}}{\partial t} \sim -P\left[\frac{\partial u_i}{\partial x_j} + \frac{\partial u_j}{\partial x_i}\right] \equiv -P\mathcal{S}_{ij}, \tag{5}$$

where $\mathcal{S}$ is the stress tensor of the bulk stirring flow. In our case, this can be obtained from Equation (1). Equation (5) reveals an important property, namely, that the velocity distribution function will be distorted along the principal axes of the stress tensor; that is, the temperature anisotropy results from the topology of the vortical Taylor–Green flow.

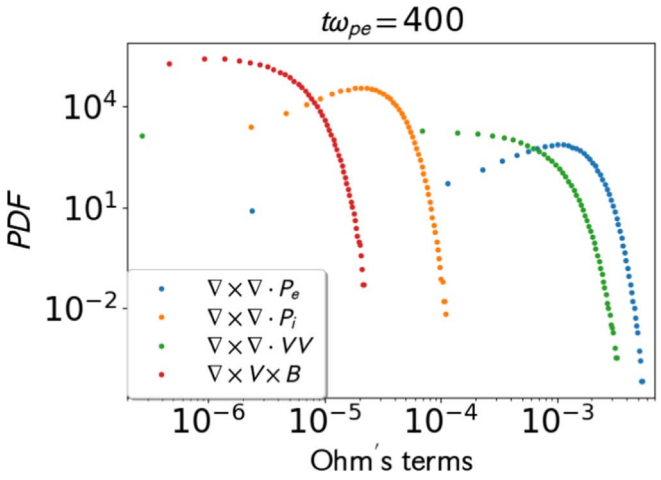


**Figure 3.** PDF of the induction equation terms given by Equation (3) at time $400\omega_{\rm pe}^{-1}$.

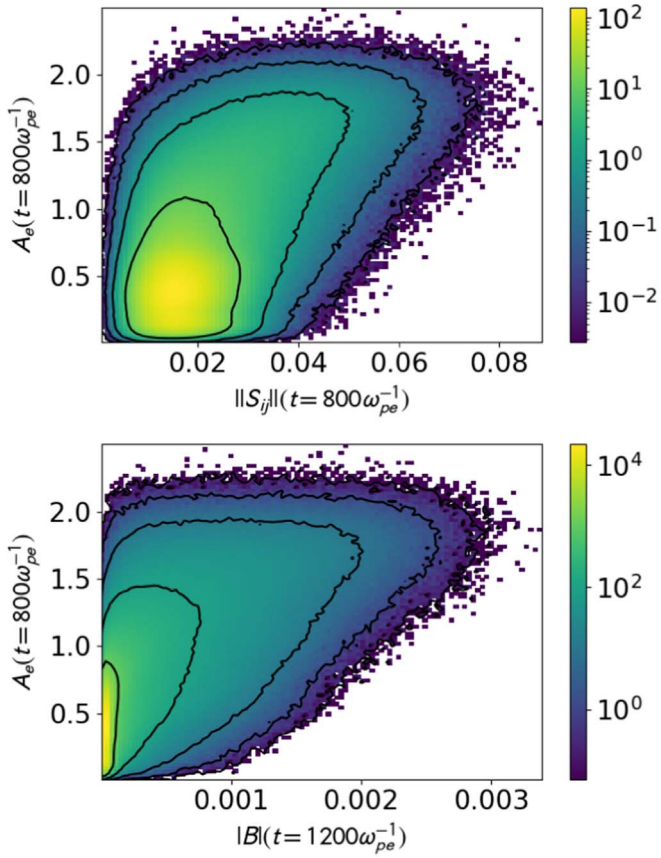


**Figure 4.** 2D histograms. Top: norm of the stress tensor and electron anisotropy at time $t = 800\omega_{\rm pe}^{-1}$. Bottom: magnetic field module at time $t = 1200\omega_{\rm pe}^{-1}$ and electron anisotropy at the earlier time $t = 800\omega_{\rm pe}^{-1}$. The black lines indicate the decades in the color bars.

To validate this model, we computed the 2D, joint distributions between the anisotropy and the stress tensor. For the stress tensor, we calculated its Frobenius norm, or second invariant, $||\mathcal{S}|| = \sqrt{Tr\{\mathcal{S}\mathcal{S}^T\}}$, where Tr indicates the trace of the matrix. In Figure 4 we observe that $A_e$ and $\mathcal{S}$ are correlated. We computed this correlation at the earliest stages, namely, at $t\omega_{\rm pe} \sim 800$, but the picture is similar at any time that precedes the anisotropy collapse in Figure 1. Analogously, to establish

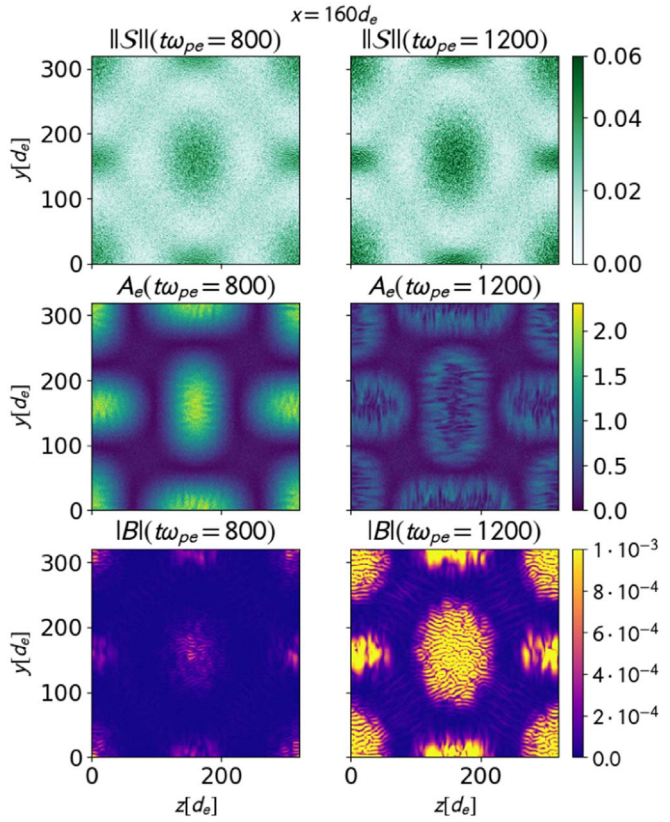


**Figure 5.** 2D shaded contour, at the center of the box $x = 10d_i$, for stress tensor strength (top), electron temperature anisotropy (middle), and magnetic field (bottom). Left and right columns refer to $t\omega_{pe} = 800$ and 1200, respectively.

the causality of the processes, we computed the joint distributions built on $A_e$ and $|\boldsymbol{B}|$: at a given time, high values of the magnetic field are located in regions where the temperature anisotropy was previously large. This joint PDF is reported in Figure 4 (bottom).

The above picture can be recovered locally, by looking at 2D cuts in space. In Figure 5 we report $A_e$, $|\boldsymbol{B}|$, and $||\mathcal{S}_{ij}||$ in the middle of the domain. High $\mathcal{S}$ generates $A_e$. After the latter reaches its maximum, the electron pressure isotropizes, giving birth to the magnetic field. The missing step is now to confirm the role of the Weibel instability in this dynamics.

We summarize the main ingredients of the electron–Weibel instability (Weibel 1959). For a system where $T_\parallel \equiv T_1 > T_\perp \equiv T_2 \equiv T_3$, $\boldsymbol{k} = k\hat{\boldsymbol{e}}_2$, $\boldsymbol{E} = E\hat{\boldsymbol{e}}_1$, and $\boldsymbol{B} = B\hat{\boldsymbol{e}}_3$, and where the initial state is defined by a bi-Maxwellian perturbed by $f = f_1 \exp\{i(kx_2 - \omega t)\}$, the dispersion relation becomes (Krall & Trivelpiece 1973)

$$d_e^2 k_y^2 - \frac{\omega^2}{\omega_{\rm pe}^2} + a_e + (a_e + 1)\xi\zeta(\xi) = 0, \qquad (6)$$

where $\zeta(\xi)$ is the plasma dispersion function, $\xi = \frac{\omega}{k_y v_\perp}$, $u = \frac{v_y}{v_\perp}$, and $a_e = \frac{v_\parallel^2}{v_\perp^2} - 1$. Note that the latter is equivalent to the temperature anisotropy in the minimum variance frame $A_e$, defined in Equation (2). We solved Equation (6) by looking for complex roots of the type $\omega = i\gamma$, using the parameters of our numerical experiment. We show the time evolution of the fastest-growing mode, which we measured as $k_0 = 0.61 d_e^{-1}$ from Figure 1 (bottom). In Figure 6 we report the time history

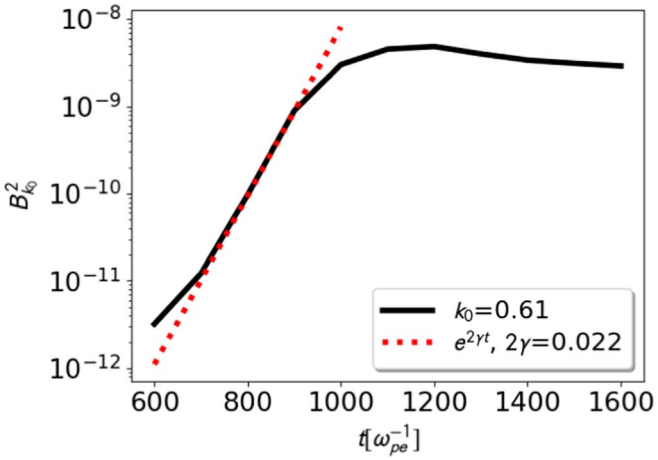


**Figure 6.** Growth rate of the Weibel instability for the fastest-growing mode $k_0 = 0.61$. The red line is the fit to the exponential growth phase.

of this mode, which grows exponentially in time and then saturates. From the exponential fit we get $\gamma = 0.011$. The Weibel theoretical growth rate is obtained using $v_\perp = v_{{\rm th},e}$ and $a_e = 2$, the latter being close to the maximum value shown in Figures 4 and 5. These parameters give $\gamma_{\rm th} = 0.015$, in agreement with our numerical result.

## 4. Discussion and Conclusion

In this Letter, we demonstrated that a magnetic field can be generated by shearing motions typical of turbulent fields, via an electron–Weibel instability. Our initial condition is meant to mimic any vortical motion, such as the eddy interaction in convective cells or the turbulence that may develop in coherent shearing motions triggered by gravitational perturbations (Pariev & Colgate 2007; Pariev et al. 2007). The stresses generated at the intersection of the rotating vortexes produce pressure anisotropy, qualitatively in accord with Equations (4)–(5). The ions, being heavier, are slow and play very little role in the early system dynamics. On the other hand, the lighter electrons interact faster with the fields, generating a Weibel instability that, in turn, induces exponential growth of the magnetic field. This hypothesis is supported by our analysis of Ohm's law, where the divergence of the electron pressure is the dominant term. As shown in Figure 5, the electron anisotropy at two consecutive times shows the imprint of the magnetic field generation. The theoretical growth rate matches well with the most energetic mode emerging the simulation. Such a mechanism provides a plausible explanation for the origin of the seed magnetic field necessary for dynamo theories. We note that the results shown were initiated with $T_i/T_e = 5$, a choice of parameters that makes electron-pressure-driven magnetogenesis more difficult to achieve. In this sense, our parameter choice is relatively conservative. Variation of this and other parameters is left for future study. Also note that numerically determined values of $v_{\rm th}/c$ are not realistic, but the corresponding Mach numbers are reasonable (Elmegreen & Scalo 2004); the scale over which the process is presumed to operate, $10d_i$, is more extreme in astrophysical terms, but is chosen here to demonstrate the magnetogenesis mechanism in reasonable timescales using necessarily finite numerical resources.

We can understand the timescales involved in this problem as follows. Clearly, both the initial correlation scale $\ell$ and the electron inertial scale $d_e$ are controlling parameters. The Taylor–Green dynamics, initially contained at scale $\ell$, will produce small-scale gradients down to $d_e$ within an eddy turnover time (see, e.g., Van Dyke 1975). Therefore, following Equation (5), strong anisotropies will be produced on the same scale, thus triggering the Weibel instability. The consistency of this picture is easily inferred from the growth of anisotropy and magnetic field energy in Figure 1. The first follows the "slower" convective timescale of order $1000\omega_{\rm pe}^{-1}$, while the second (see also Figure 6) follows the Weibel timescale of order $100\omega_{\rm pe}^{-1}$. This implies that in a more realistic scenario having a larger $\ell/d_e$ ratio, it is turbulence that determines the magnetogenesis triggering. These seeds of anisotropy and primordial magnetic field will clearly sprout in randomly distributed locations where gradients are favorable for the production through the above process.

We have demonstrated that kinetic processes can produce a seed magnetic field that begins with anisotropies at electron scales. Our results also show (see Figure 1) that magnetic energy also rapidly increases at ion scales, an effect that will be sustained if the process is continuously driven, in a more realistic circumstance. Once the magnetic energy reaches ion scales the problem of producing observable magnetic fields at the required scales of tens of parsecs is relegated to a sequence of ion-scale instabilities in concert with classical dynamo action (Rincon 2019). These can presumably span the 12 orders of magnitudes of scale from the electron inertial scale, where the presently demonstrated magnetogenesis operates, to the observed scales in which cosmic magnetic fields are observed (Parker 1979).

During the evaluation of this Letter, a reviewer called our attention to a related work that was recently posted (Zhou et al. 2021).

This work has received funding from the European Union's Horizon 2020 Research and Innovation Program Grant 776262 (Artificial Intelligence Data Analysis; http://www.aida-space.eu/). F.P. was supported by the PostDoctoral Fellowship 12X0319N and the Research Grant 1507820N from Research Foundation—Flanders (FWO). We acknowledge the European PRACE initiative for awarding us access to the supercomputer SuperMUC-NG at GCS@LRZ, Germany. W.H.M. was partially supported by a US NSF grant PHY2108834 to the University of Delaware.

## ORCID iDs

F. Pucci https://orcid.org/0000-0002-5272-5404
M. Viviani https://orcid.org/0000-0003-3317-5889
F. Valentini https://orcid.org/0000-0002-1296-1971
G. Lapenta https://orcid.org/0000-0002-3123-4024
W. H. Matthaeus https://orcid.org/0000-0001-7224-6024
S. Servidio https://orcid.org/0000-0001-8184-2151

## References

Biermann, L. 1950, ZNatA, 5, 65
Brandenburg, A. 2018, JPlPh, 84, 735840404
Cerri, S. S., Pegoraro, F., Califano, F., Del Sarto, D., & Jenko, F. 2014, PhPl, 21, 112109
Colgate, S. A., Li, H., & Pariev, V. 2001, PhPl, 8, 2425
Del Sarto, D., Pegoraro, F., & Califano, F. 2016, PhRvE, 93, 053203
Elmegreen, B. G., & Scalo, J. 2004, ARA&A, 42, 211
Huntington, C., Fiuza, F., Ross, J., et al. 2015, NatPh, 11, 173
Kraichnan, R., & Nagarajan, S. 1967, PhFl, 10, 859
Krall, N. A., & Trivelpiece, A. W. 1973, Principles of Plasma Physics (New York: McGraw-Hill)
Kulsrud, R. M., & Zweibel, E. G. 2008, RPPh, 71, 046901
Markidis, S., Lapenta, G., & Rizwan-uddin 2010, Math. Comput. Simul., 80, 1509
Mininni, P. D., Gómez, D. O., & Mahajan, S. M. 2003, ApJ, 587, 472
Olshevsky, V., Servidio, S., Pucci, F., Primavera, L., & Lapenta, G. 2018, ApJ, 860, 11
Pariev, V. I., & Colgate, S. A. 2007, ApJ, 658, 114
Pariev, V. I., Colgate, S. A., & Finn, J. M. 2007, ApJ, 658, 129
Parker, E. N. 1970, ApJ, 162, 665
Parker, E. N. 1979, Cosmical Magnetic Fields: Their Origin and Their Activity (Oxford: Oxford Univ. Press)
Pouquet, A., Frisch, U., & Leorat, J. 1976, JFM, 77, 321
Pusztai, I., Juno, J., Brandenburg, A., et al. 2020, PhRvL, 124, 255102
Rincon, F. 2019, JPlPh, 85, 205850401
Rincon, F., Califano, F., Schekochihin, A. A., & Valentini, F. 2016, PNAS, 113, 3950
Schlickeiser, R., & Shukla, P. K. 2003, ApJL, 599, L57
Schoeffler, K. M., Loureiro, N. F., Fonseca, R. A., & Silva, L. O. 2016, PhPl, 23, 056304
Schoeffler, K. M., & Silva, L. O. 2020, PhRvR, 2, 033233
Servidio, S., Valentini, F., Califano, F., & Veltri, P. 2012, PhRvL, 108, 045001
St-Onge, D. A., & Kunz, M. W. 2018, ApJL, 863, L25
St-Onge, D. A., Kunz, M. W., Squire, J., & Schekochihin, A. A. 2020, JPlPh, 86, 905860503
Taylor, G. I., & Green, A. E. 1937, RSPSA, 158, 499
Van Dyke, M. 1975, SJAM, 28, 720
Weibel, E. S. 1959, PhRvL, 2, 83
Widrow, L. M., Ryu, D., Schleicher, D. R. G., et al. 2012, SSRv, 166, 37
Zhou, M., Zhdankin, V., Kunz, M. W., Loureiro, N. F., & Uzdensky, D. A. 2021, arXiv:2110.01134